An *n*-doped organic layer assists the anode modification of inverted organic solar cell for the efficiency improvement

Shang Feng[1] · Hailiang Zhao[1] · Qingqing Yang[2] · Jidong Zhang[2] · Dashan Qin[1]

Abstract

Inverted organic solar cells have been fabricated with an anode modifying bilayer, comprised of thermally evaporated MoO_3 and ytterbium *n*-doped bathocuproine (BCP:Yb). In the bilayer, MoO_3 and BCP:Yb play the roles of forming ohmic contacts with photoactive layer and anode, respectively; due to the Fermi level alignment, MoO_3 and BCP:Yb form a low-barrier interface, benefiting hole injection and extraction. The MoO_3/BCP:Yb bilayer enables higher open-circuit voltage of inverted device than the conventional MoO_3 layer, mostly because BCP:Yb suppresses the reduction of MoO_3 work function by anode. Moreover, the introduction of BCP:Yb helps increase the optical absorption of inverted device and thereby short-circuit current density. Although BCP:Yb gives increased electron mobility than MoO_3, the MoO_3/BCP:Yb bilayer decreases hole mobility of inverted device and thereby fill factor than the MoO_3 layer, mostly due to the interfacial *p*-doping effect of MoO_3 on BCP:Yb. The power conversion efficiency based on MoO_3/BCP:Yb bilayer is 6.60%, higher than that (6.25%) based on the MoO_3 layer. The current research indicates that *n*-doped organic layers are helpful to improve the efficiencies of inverted OSCs via assisting the anode modification.

1 Introduction

Organic solar cells (OSCs) as an emerging photovoltaic technology have attracted world-wide attention [1–10], because of their superiorities of light weight, flexibility, and environment-friendly fabrication. Owing to the tremendous progresses of material science and device engineering [11, 12], state-of-the-art OSCs have achieved the level of 19–20% for power conversion efficiency (PCE) [6, 9]. To enter the commercial photovoltaic market in the near future, however, OSCs need to reach higher PCEs and realize the maximum cost-effectiveness at the same time.

The photoactive layer (PAL) is the central part of OSC, absorbing incident light to generate the excitons and then dissociating them into free carriers [13]. In general, anode and cathode modifying layers (AMLs and CMLs) are the indispensable parts for making high-efficiency OSCs, locating between anode and PAL and between cathode and PAL, respectively. The roles of AMLs (or CMLs) are as follows: (1) enhance the extraction and injection of holes (or electrons) at the interface of anode (or cathode) and PAL; (2) keep PAL from being damaged by anode (or cathode), reducing the nonradiative recombination; (3) prevent the photogenerated excitons from being quenched by anode (or cathode), suppressing the geminate recombination; (4) optimize the distribution of optical field of incident light to increase the optical absorption of device [14]. Obviously, the AMLs and CMLs are vital to the efficiency and operational stability of OSCs.

In inverted OSCs, surface-modified ZnO thin films have been often used as CMLs to enable high PCE, production yield, and operational stability [15, 16]. The most frequently applied AMLs are thermally evaporated MoO_3 and solution-processed poly(3,4-ethylenedioxythiophene):poly(styrenesulfonate) (PEDOT:PSS) and its derivatives [17–19].

✉ Dashan Qin
  qindashan06@aliyun.com

1 Hebei Key Laboratory of Functional Polymers, School of Chemical Engineering, Hebei University of Technology, Tianjin 300401, People's Republic of China

2 State Key Laboratory of Polymer Physics and Chemistry, Changchun Institute of Applied Chemistry, Chinese Academy of Sciences, Changchun 130023, Jilin, People's Republic of China

It is reported that alcohol-dispersed PEDOT:F shows similar electrical properties, i.e., work function (WF) and conductivity, to water-dispersed PEDOT:PSS, but higher PCE and operational stability of inverted device, mostly due to the lower acidity and surface tension of PEDOT:F than those of PEDOT:PSS [17]. Moreover, the PEDOT:F shows comparable performance of inverted device to thermally evaporated MoO_3. From the production point of view, the AMLs need be capable to well smooth PAL, thereby ensuring high production yield of large-area inverted OSCs [20]. As yet, it still remains uncertain what is the minimum thickness for solution processed AMLs to realize high production yield of inverted OSCs with large area, for example, 274.5 cm^2. Whereas, large-area organic thin films thermally evaporated grow uniform, continuous, and pinhole-free even at low thickness (~ 10 nm). For example, the glass substrate dimension for the commercial 6th generation AMOLED thermal-evaporation production line is 1.50×1.85 m^2. Therefore, it is of importance and value to develop thermally evaporated AMLs towards the low-cost fabrication of large-area inverted OSCs.

The MoO_3 is a kind of *n*-type material and performs as a high-performance AML due to its high WF [21]. However, the commercial application of thermally evaporated MoO_3 is retarded by the following two shortcomings: (1) the low electron mobility of MoO_3 limits the fill factor (FF) of device [22]; (2) the reduction of MoO_3 WF by anode decreases open-circuit voltage (V_{OC}) of device [23]. Recently, polyethylenimine ethoxylated (PEIE) has been reported to assist MoO_3 in improving the performance of inverted OSC [23]. Regretfully, PEIE is an insulator and also causes severe decomposition of nonfullerene acceptors [24], thus restricting the commercial application of the MoO_3/PEIE bilayer. It should be emphasized that, although *n*-doped organic layers function as CMLs in OSCs, e.g., ytterbium doped bathophenanthroline [25, 26], none of them have been ever tried to assist the anode modification in OSCs for the efficiency enhancement.

Herein, thermally evaporated ytterbium-doped bathocuproine (BCP:Yb) has been employed to assist MoO_3 in enhancing the performance of inverted OSC. In the MoO_3/BCP:Yb bilayer, MoO_3 forms ohmic contact with PAL and BCP:Yb forms ohmic contact with anode; due to the Fermi level alignment, MoO_3 and BCP:Yb form a low-barrier contact. The current research provides a new insight to design anode modification and develop AMLs for inverted OSCs.

2 Experimental

2.1 Materials

Poly[4,8-bis(5-(2-ethylhexyl)thiophen-2-yl)benzo[1,2-b;4,5-b′]dithiophene-2,6-diyl-alt-(4-(2-ethylhexyl)-3-fluorothieno[3,4b]thiophene-)-2-carboxylate-2–6-diyl)] (PTB7-Th) and [6, 6]-phenyl C_{71}-butyric acid methyl ester ($PC_{71}BM$) were purchased from Solarmer Materials Inc. Regioregular poly(3-hexylthiophene) (P3HT) and [6, 6]-phenyl-C_{61}-butyric acid methyl ester ($PC_{61}BM$) were bought from Rieke Metals and Xi'an Polymer Light Technology Corp, respectively. Poly(3,4-ethylenedioxythiophene):poly(styrenesulfonate) (PEDOT:PSS, CLEVIOS™ P AI4083) was adopted. Polyethylenimine ethoxylated (PEIE, 80% ethoxylated, Mw 110,000 g mol^{-1}, and 37wt.% in water) and MoO_3 were obtained from Sigma-Aldrich company. The BCP was obtained from Jilin OLED Material Tech Co., Ltd. All the materials were used as received. The glass substrates coated with 100 nm thick indium tin oxide (ITO) with sheet resistance = 15 Ω^{-2} were applied.

2.2 Device fabrication and measurements

The CML of ZnO thin film (*ca*. 30 nm) was spin-coated onto ITO glass for 40 s at a speed of 4000 rpm from a ZnO precursor solution, which was 100 mg mL^{-1} zinc acetate dihydrate solution using mixed 2-methoxyethanol and ethanolamine (97:3 by volume), and then annealed at 200 °C for 30 min under ambient condition. The PAL of PTB7-Th:$PC_{71}BM$ (*ca*. 110 nm) was spin-coated onto ZnO for 30 s at a speed of 1100 rpm from a dichlorobenzene/1,8-diiodooctane (97:3 by volume) solution containing 10 mg mL^{-1} PTB7-Th and 15 mg mL^{-1} $PC_{71}BM$. The CML of PEIE (*ca*. 5 nm) was spin-coated onto ITO glass for 60 s at a speed of 5000 rpm from a 0.2 wt.% PEIE solution dissolved in methanol. The PAL of P3HT:$PC_{61}BM$ was spin-cast onto PEIE for 30 s at a speed of 1000 rpm from a mixed 12 mg mL^{-1} P3HT and 10 mg mL^{-1} $PC_{61}BM$ solution using 1,2-dichlorobenzene. As-cast P3HT:$PC_{61}BM$ thin film appeared orange and became deep purple when the residual solvent was evaporated completely. The time scale for the color of blend thin film changing from orange to deep purple was defined as solvent-evaporation time. All the solution-processed thin films were made in the air. The AMLs of MoO_3, BCP:Yb (by mass ratio), and BCP were thermally evaporated onto PAL in the vacuum chamber with a base pressure of 5×10^{-4} Pa. The active area of device was defined to be 2×2 mm^2 by patterning the thermal evaporation of Al cathode with thickness of 100 nm via shadow mask.

For measuring electron mobility (μ_e) of MoO_3 or BCP:Yb (10:4), the electron-only device with structure of ITO/70 nm MoO_3 or BCP:Yb (10:4)/Al was fabricated. For measuring hole mobility (μ_h) of inverted OSCs, the hole-only devices with structure of ITO/PEDOT:PSS/PTB7-Th:$PC_{71}BM$/AML/Al were made, where AML = 10 nm MoO_3 and 5 nm MoO_3/5 nm BCP:Yb (10:4), respectively. The PEDOT:PSS (*ca*. 30 nm) was spin-cast onto ITO glass at a speed of 4000 rpm for 30 s and then baked at 80 °C for 30 min.

Table 1 The complex refractive indexes for ITO, ZnO, PTB7-Th:PC$_{71}$BM, MoO$_3$, BCP, and Al at different wavelengths

Wavelength(nm)	ITO	ZnO	PTB7-Th:PC$_{71}$BM	MoO$_3$	BCP	Al
400	$2.12 + i\,0.044$	$1.69 + i0.015$	$1.86 + i\,0.024$	$1.96 + i0.028$	1.80	$0.57 + i\,5.015$
500	$1.97 + i\,0.043$	$1.63 + i0.004$	$1.86 + i\,0.262$	$1.88 + i0.007$	1.80	$0.71 + i\,6.236$
600	$1.88 + i\,0.054$	$1.63 + i0.019$	$1.87 + i\,0.281$	$1.83 + i0.003$	1.80	$1.18 + i\,7.445$
700	$1.82 + i\,0.066$	$1.62 + i0.001$	$2.05 + i\,0.387$	$1.81 + i0.001$	1.80	$2.01 + i\,8.358$

The data for ITO, BCP, and Al are obtained from Ref. [28]. The data for PTB7-Th:PC$_{71}$BM are gotten from the Ref. [29]. The data for ZnO and MoO$_3$ are taken from Ref. [30]

Mobility was extracted by fitting the current density versus voltage (*J–V*) curves of hole- and electron-only devices using the Mott–Gurney law incorporating the electric field dependence of mobility [27].

The *J–V* characteristics of inverted OSCs under the 1 sun simulated AM 1.5G illumination (CXE-400 arc Xe lamp) and hole- and electron-only devices were recorded by a programmable Keithley 2400 DC sourcemeter in the air. The thicknesses of spin-coated thin films were measured using Bruker DektakXT stylus profiling system. The UV–Vis absorption measurements were carried out using a Cary 300 spectrophotometer. The morphologies of samples were recorded using a Digital Instruments Nanoscope IIIa multimode atomic force microscope (AFM) in tapping mode. The

X-ray photoelectron spectroscopy (XPS) measurements were done on an X-ray photoelectron spectrometer (ESCALAB 250Xi). Typically, the hydrocarbon C 1 s line at 284.8 eV from adventitious carbon was used for energy reference.

2.3 Optical modeling

The intensity distributions of incident-light optical field in inverted OSCs were simulated using Wave Optics Module of COMSOL Multiphysics, based on the Fluent periodic boundary conditions and the inclusion of perfectly matched layers in the device model. The complex refractive indexes for ITO, ZnO, PTB7-Th:PC$_{71}$BM, MoO$_3$, BCP, and Al at the wavelengths of 400, 500, 600, and 700 nm were summarized

Fig. 1 The molecular structures of PTB7-Th, PC$_{71}$BM, P3HT, PC$_{61}$BM, PEDOT:PSS, PEIE, and BCP
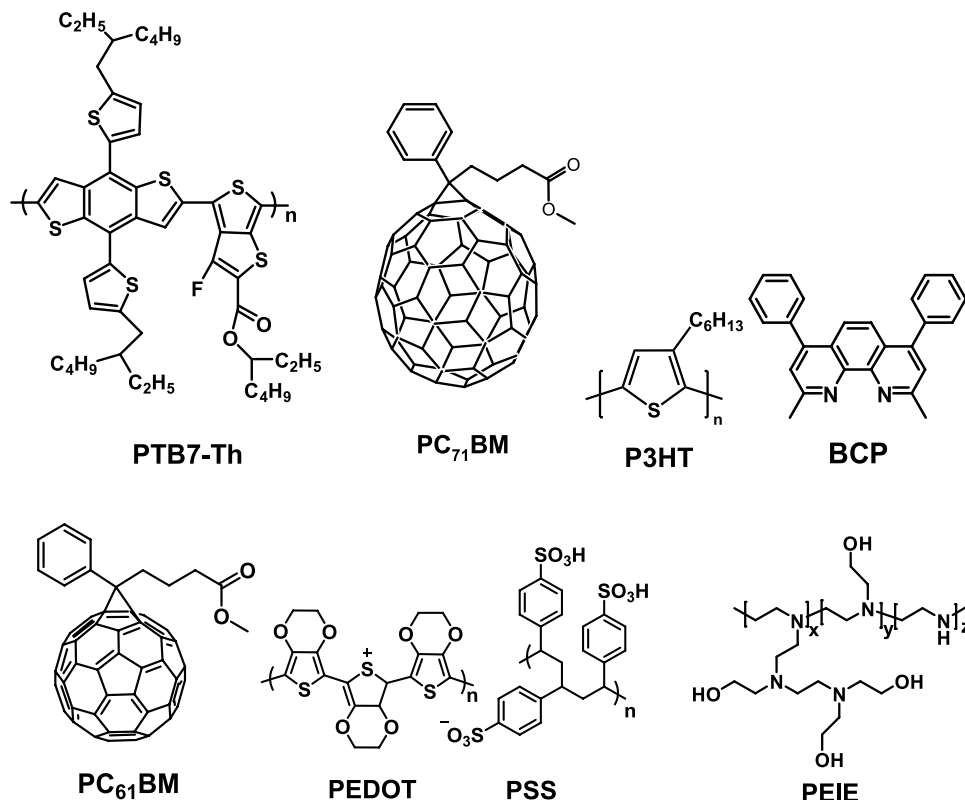
Table 2 The photovoltaic performance data of ITO/ZnO/PTB7-Th:PC$_{71}$BM/AML/Al, where AML = 10 nm MoO$_3$, 5 nm MoO$_3$/5 nm BCP:Yb (10:4), and 5 nm MoO$_3$/5 nm BCP, respectively

AML	V_{SC} (V)	J_{SC} (mA cm^{-2})	FF	PCE (%)	$R_S{}^a$ (Ω cm^2)
MoO$_3$	0.78 ± 0.00 (0.78)	15.52 ± 0.63 (16.46)	0.52 ± 0.02 (0.52)	6.25 ± 0.26 (6.62)	9.77 ± 0.89
MoO$_3$/BCP:Yb	0.80 ± 0.01 (0.80)	16.46 ± 0.59 (17.11)	0.50 ± 0.01 (0.50)	6.60 ± 0.22 (6.78)	11.23 ± 0.79
MoO$_3$/BCP	0.70 ± 0.03 (0.73)	10.14 ± 1.28 (11.71)	0.37 ± 0.02 (0.39)	2.67 ± 0.49 (3.34)	30.45 ± 6.41

Average values with standard deviation for each structure are obtained from 10 devices. For each AML, the numbers in the brackets are obtained from the device with best PCE

[a]The R_S stands for series resistance, estimated by calculating the inverse of the slope of J–V curve at the V_{OC} point

in Table 1. The BCP:Yb thin film was treated as Yb clusters with 1 nm diameter uniformly distributed in BCP thin film.

3 Results and discussion

3.1 The performance comparison of inverted OSCs

Figure 1 shows the molecular structures of PTB7-Th, PC$_{71}$BM, P3HT, PC$_{61}$BM, PEDOT:PSS, PEIE, and BCP.

(a)

| Al anode |
|---|
| AML |
| PTB7-Th:PC$_{71}$BM |
| ZnO |
| ITO cathode |

(b)
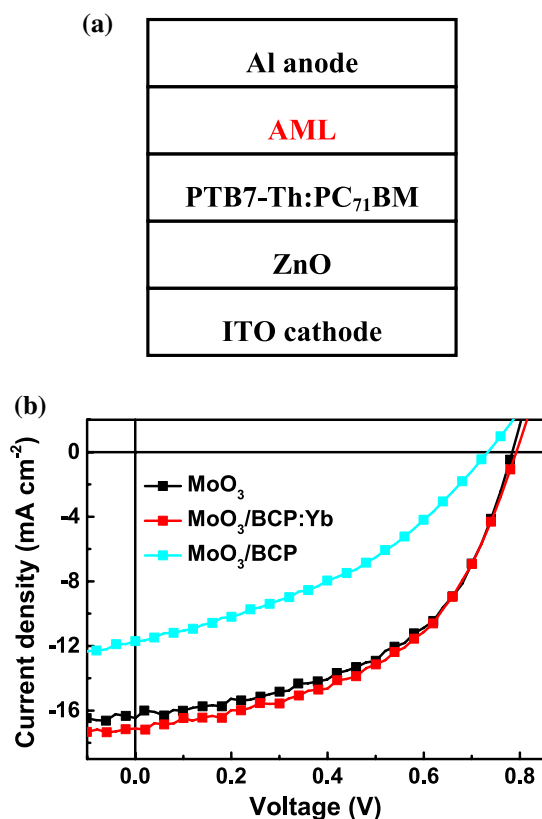
Fig. 2 The architecture **a** and illuminated J–V characteristics **b** of inverted OSCs with structure of ITO/ZnO/PTB7-Th:PC$_{71}$BM/AML/Al, where AML = 10 nm MoO$_3$, 5 nm MoO$_3$/5 nm BCP:Yb (10:4), and 5 nm MoO$_3$/5 nm BCP, respectively

Figure S1 and Table S1 show that for the anode modifying bilayer of MoO$_3$/BCP:Yb, the optimal mass ratio of BCP to Yb is ∼ 10:4, delivering the highest PCE for inverted OSC with structure of ITO/PEIE/P3HT:PC$_{61}$BM/5 nm MoO$_3$/5 nm BCP:Yb/Al. Fig. S2 displays that the inverted OSC of ITO/PEIE/P3HT:PC$_{61}$BM/5 nm BCP:Yb (10:4)/Al gives almost no photovoltaic performance, indicating BCP:Yb (10:4) is unable to modify the PAL/anode interface alone, mostly because the WF (3.2 eV) of BCP:Yb does not match the ionization energy (IP, 5.2 eV) of PTB7-Th.

To demonstrate the advantages of the MoO$_3$/BCP:Yb bilayer over the conventional MoO$_3$ layer in terms of anode modification, three inverted OSCs with structure of ITO/ZnO/PTB7-Th:PC$_{71}$BM/AML/Al are made as shown in Fig. 2a, where AML = 10 nm MoO$_3$, 5 nm MoO$_3$/5 nm BCP:Yb (10:4), and 5 nm MoO$_3$/5 nm BCP, respectively. The illuminated J–V characteristics and detailed photovoltaic parameters of these three inverted OSCs are presented in Fig. 2b and Table 2, respectively. The inverted OSC with 5 nm MoO$_3$/5 nm BCP:Yb (10:4) shows higher V_{OC} and J_{SC} but lower FF and series resistance than the one with 10 nm MoO$_3$. The PCE (6.60%) based on the 5 nm MoO$_3$/5 nm BCP:Yb (10:4) bilayer is higher than that (6.25%) based on the 10 nm MoO$_3$ layer, indicating that the BCP:Yb (10:4) is
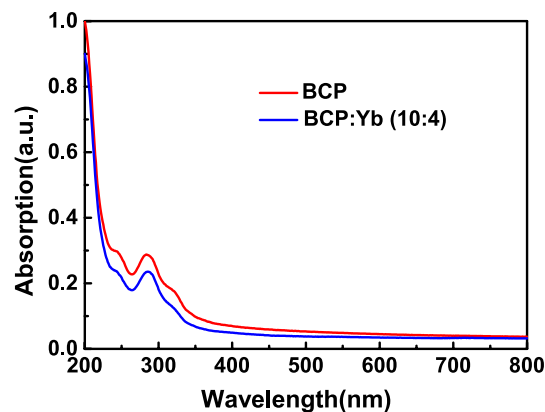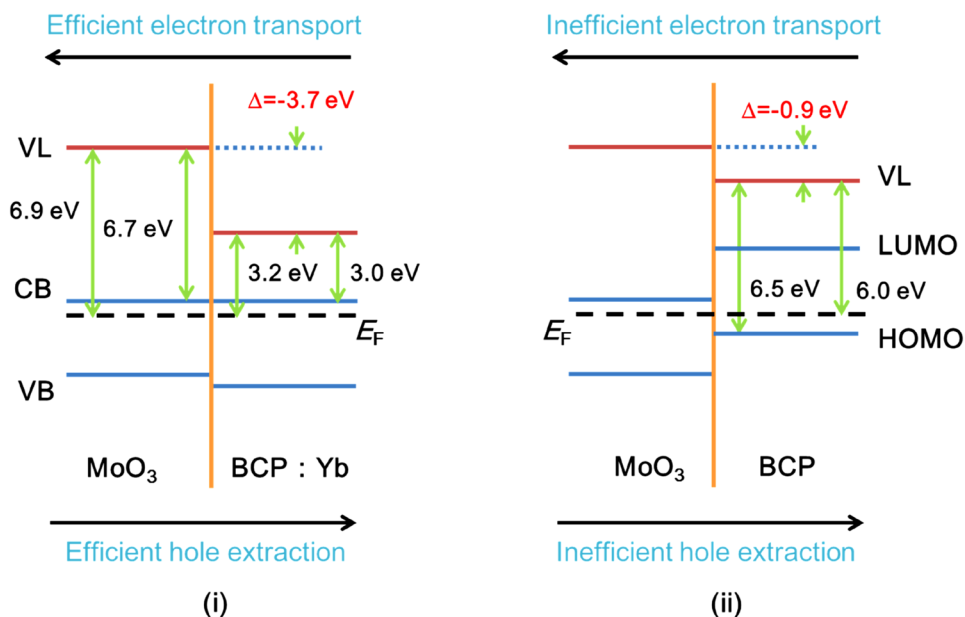

Fig. 3 The optical absorption spectra of 20 nm BCP and BCP:Yb (10:4) thin films deposited on quartz glass
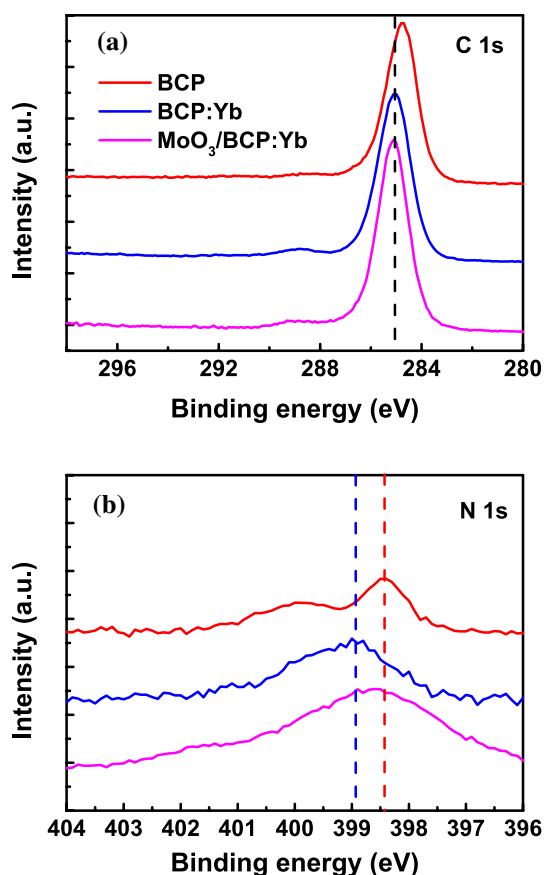
Fig. 4 XPS spectra of C 1 s **a** and N 1 s **b** core levels for glass/20 nm BCP, glass/ 20 nm BCP:Yb (10:4), and glass/5 nm MoO_3/5 nm BCP:Yb (10:4)

able to assist MoO_3 with the anode modification in inverted OSC. It is worth noting that the inverted OSC with 5 nm MoO_3/5 nm BCP shows much deteriorated photovoltaic parameters than its two counterparts based on 10 nm MoO_3 and 5 nm MoO_3/5 nm BCP:Yb (10:4).

3.2 The electrical properties of BCP:Yb

Figure 3 displays that the long-wavelength edge of absorption spectrum for BCP:Yb (10:4) is slightly blue-shifted, compared to that for BCP, indicating the spontaneous electron transfer from Yb to BCP [31, 32]. This is an energetically favorable process, since the WF (2.6 eV) of Yb as *n*-type dopant is very close to the electron affinity (EA, 3.0 eV) of BCP as *n*-type matrix [33, 34]. Figure 4 investigates the chemical interaction between BCP and Yb. It can be seen that the XPS signals of C 1 s and N 1 s for BCP:Yb (10:4) shift to higher binding energies, compared to those for BCP, indicating the chemical bonding of Yb with C and N in Bphen and thereby confirming the *n*-doping effect of Yb in BCP [26, 35]. Figure S3 indicates that the μ_e of BCP:Yb (10:4) is calculated to be 3.9×10^{-4} cm^2 V^{-1} s^{-1}, much higher than the reported value (5.5×10^{-6} cm^2 V^{-1} s^{-1}) of BCP [36], mostly ascribed to that the increase of free electrons caused by *n*-doping gets more traps filled in BCP:Yb (10:4), as compared to in BCP.

Fig. 5 The energy level alignments at the MoO_3/BCP:Yb i and MoO_3/BCP ii interfaces. The VL, CB, VB, HOMO, LUMO, E_F, and Δ stand for vacuum level, the bottom of conduction band, the top of valence band, highest occupied molecular orbital, lowest unoccupied molecular orbital, Fermi level, and interfacial dipole, respectively. For simplicity, the band bending is neglected at the interfaces. Note that, in both i and ii, when the electrons are transported from right to left, it is equal to the hole extraction towards anode
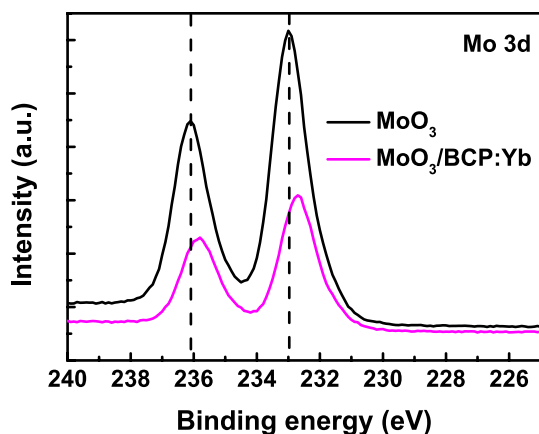
Fig. 6 XPS spectra of Mo 3d core levels for glass/10 nm MoO$_3$ and glass/5 nm MoO$_3$/5 nm BCP:Yb (10:4)

### 3.3 The anode-modifying mechanism of the MoO$_3$/BCP:Yb bilayer

The energy levels of the MoO$_3$/BCP:Yb (10:4) and MoO$_3$/BCP bilayers are suggested in Fig. 5. The IP of 9.7 eV, EA of 6.7 eV, and WF of 6.9 eV are taken for MoO$_3$ [21], and the IP of 6.5 eV, EA of 3.0 eV, and WF of 3.2 eV are taken for BCP:Yb (10:4). Figure 5i shows, due to Fermi level alignment, an interfacial dipole of -3.7 eV is formed at the interface of MoO$_3$ and BCP:Yb, leading to an interfacial barrier of ~0 eV for electron transport. The electron injection

from Al to BCP:Yb is efficient via tunneling, because there is formed an very thin depletion layer between metal and n-doped layer [37]. Thus, the electrons can be efficiently transported from Al into MoO$_3$ via BCP:Yb, giving rise to efficient hole extraction.

Figure 5ii demonstrates, because MoO$_3$'s Fermi level has to be pinned at the positive inter charge-transfer state (E_{ICT+}, ~6.0 eV) of BCP [38], an interfacial dipole of -0.9 eV is resulted at the interface of MoO$_3$ and BCP, leading to a large interfacial barrier of 2.8 eV for electron transport. Hence, despite the efficient electron injection from Al to BCP [10, 34, 39], the electrons cannot be efficiently transported from Al into MoO$_3$ via BCP, leading to inefficient hole extraction. Figure 5 explains why the 5 nm MoO$_3$/5 nm BCP:Yb (10:4) bilayer increases the performance of inverted OSCs than the 5 nm MoO$_3$/5 nm BCP bilayer.

As shown in Fig. 4a, the XPS signals of C 1 s for BCP:Yb (10:4) and MoO$_3$/BCP:Yb (10:4) have same binding energies. But, as seen in Fig. 4b, the XPS signal of N 1 s for MoO$_3$/BCP:Yb (10:4) shifts to slightly lower binding energy compared to that of BCP:Yb (10:4), implying a certain electron transfer from N of BCP:Yb to MoO$_3$, here called the interfacial p-doping effect of MoO$_3$ on BCP:Yb. This is coincident with the observation in Fig. 6 that the XPS peaks of Mo 3d for MoO$_3$/BCP:Yb (10:4) shift to lower binding energies, relative to those for MoO$_3$. The interfacial p-doping effect of MoO$_3$ reduces the number of free electrons in BCP:Yb (10:4), increasing the WF of BCP:Yb (10:4) and thereby the barrier for electron transport at the MoO$_3$/BCP:Yb (10:4) interface.

Fig. 7 The normalized electric component of transverse magnetic polarized light for normal-incidence monochromatic illumination at wavelengths of 400, 500, 600, and 700 nm for ITO/ZnO/PTB7-Th:PC$_{71}$BM/AML/Al, where AML = 10 nm MoO$_3$ and 5 nm MoO$_3$/5 nm BCP:Yb (10:4), respectively
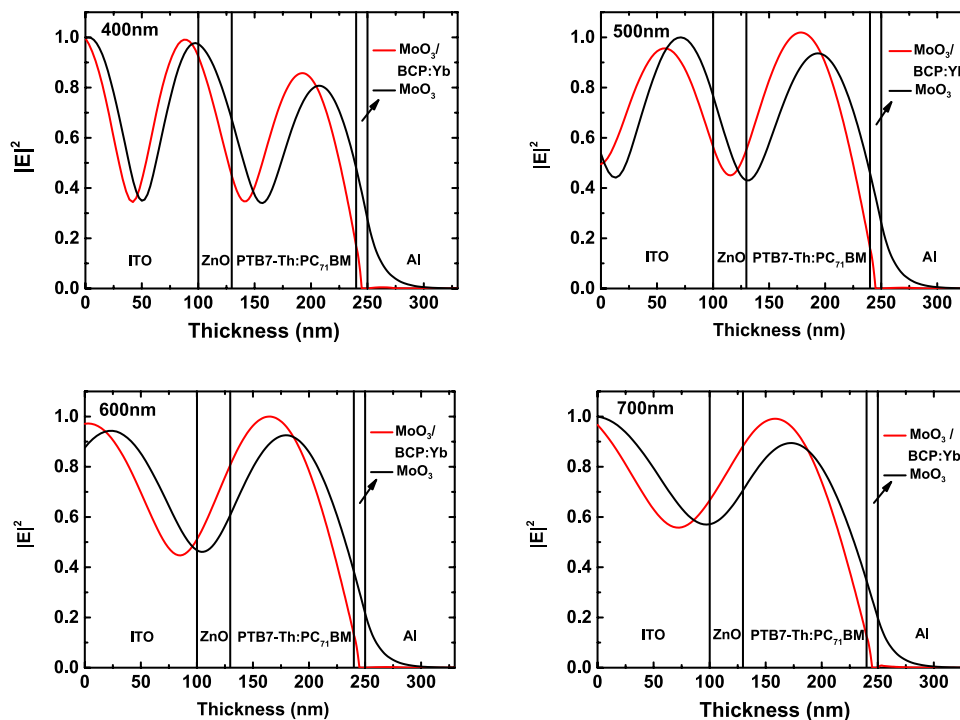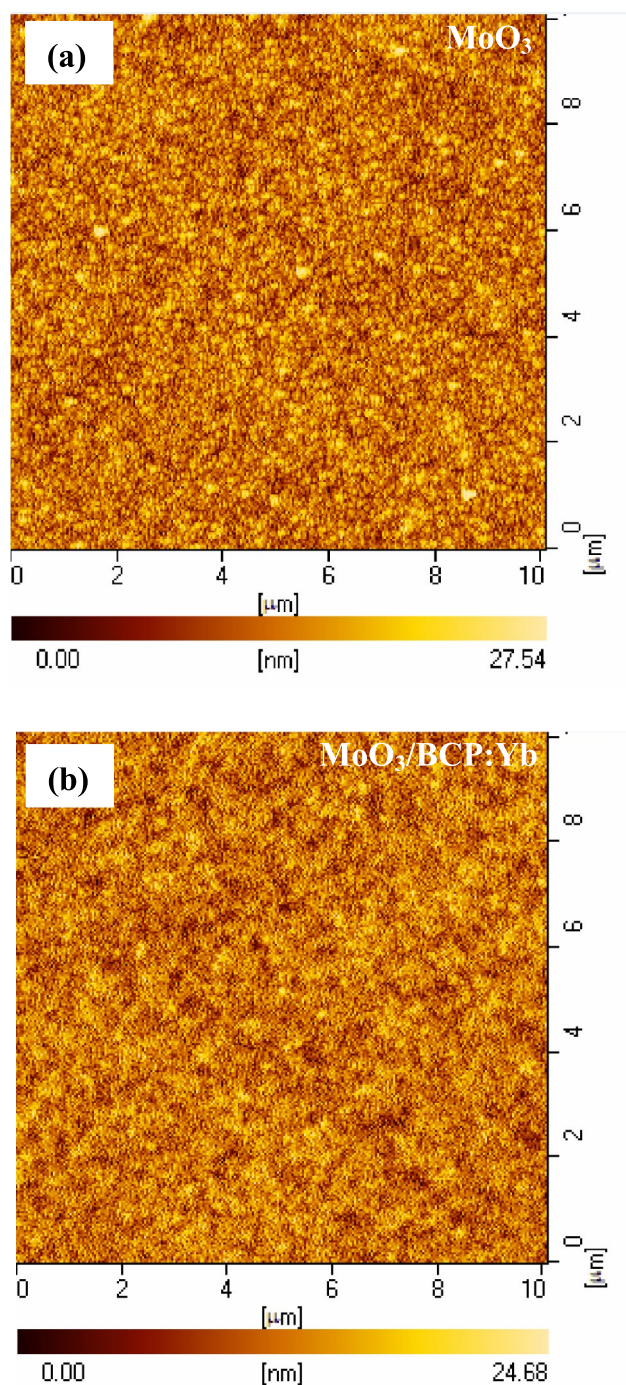
Fig. 8 AFM morphological images for the samples of ITO/ZnO/PTB7-Th:PC$_{71}$BM/AML, where AML=10 nm MoO$_3$ **a** and 5 nm MoO$_3$/5 nm BCP:Yb (10:4) **b**, respectively

Therefore, the μ_h (6.8×10^{-4} cm^2 V^{-1} s^{-1}) for the inverted OSC with the 5 nm MoO$_3$/5 nm BCP:Yb (10:4) bilayer is decreased than that (9.7×10^{-4} cm^2 V^{-1} s^{-1}) for the inverted OSC with the 10 nm MoO$_3$ layer (Fig. S4), though the μ_e (2.3×10^{-5} cm^2 V^{-1} s^{-1}) of MoO$_3$ is measured smaller than that of BCP:Yb (10:4) (Fig. S3). The

XPS signal of Yb 4d for BCP:Yb (10:4) and MoO$_3$/BCP:Yb (10:4) have same binding energies (Fig. S5), indicating that there is no chemical interaction between Yb and MoO$_3$.

3.4 The advantages of MoO$_3$/BCP:Yb (10:4) bilayer over MoO$_3$

It is reported that the cathode deposition reduces the WF of MoO$_3$, thereby decreasing V_{OC} of inverted device [23]. For the MoO$_3$/BCP:Yb (10:4) bilayer, BCP:Yb (10:4) protect MoO$_3$ from the attack of Al, thereby maintaining the WF of MoO$_3$. Therefore, the inverted OSC with the 5 nm MoO$_3$/5 nm BCP:Yb (10:4) bilayer shows higher V_{OC} than the one with the 10 nm MoO$_3$ layer. Figure 7 presents the calculated intensity distributions of optical field of incident light in the inverted OSCs using 10 nm MoO$_3$ and 5 nm MoO$_3$/5 nm BCP:Yb (10:4). For incident light with each of wavelengths of 400, 500, 600, and 700 nm, the maximum intensity of optical field in PAL based on 5 nm MoO$_3$/5 nm BCP:Yb (10:4) bilayer is larger than that based on 10 nm MoO$_3$ layer. This indicates that 5 nm MoO$_3$/5 nm BCP:Yb (10:4) bilayer increases the optical absorption of inverted device than 10 nm MoO$_3$ layer, explaining increased J_{SC} based on the former than that based on the latter. Figure 8 shows that the 5 nm MoO$_3$/5 nm BCP:Yb (10:4) bilayer grows smoother on PAL than the 10 nm MoO$_3$ layer, since the root-mean-square roughness (3.83 nm) for the former is smaller than that (4.17 nm) for the latter. As a result, it is conclusive that BCP:Yb (10:4) assists MoO$_3$ with the anode modification in improving the performance of inverted device, though it reduces the μ_h and thereby FF of inverted device.

4 Conclusions

A novel anode-modifying material, i.e., thermally evaporated MoO$_3$/BCP:Yb bilayer, has been used to improve the performance of inverted OSCs. The bilayer offers ohmic contacts with photoactive layer and anode and also possesses the low resistance for electron transport at the MoO$_3$/BCP:Yb interface, thereby ensuring efficient hole injection and extraction. Compared to the MoO$_3$ layer, the MoO$_3$/BCP:Yb bilayer enables higher efficiency, mostly because BCP:Yb blocks anode from reducing the work function of MoO$_3$ and simultaneously increases the optical absorption of inverted device. The current research indicates that *n*-doped organic layers are promising to assist the anode modification towards the low-cost and high-efficiency inverted OSCs.

Declarations

Conflict of interest The authors declare that they have no competing financial interests. The manuscript is approved by all authors for publication.

References

1. C.W. Tang, Appl. Phys. Lett. **48**, 183–185 (1986)
2. N.S. Sariciftci, L. Smilowitz, A.J. Heeger, F. Wudl, Science **258**, 1474–1476 (1992)
3. G. Yu, J. Gao, J.C. Hummelen, F. Wudl, A.J. Heeger, Science **270**, 1789–1791 (1995)
4. Y. Lin, J. Wang, Z. Zhang, H. Bai, Y. Li, D. Zhu, X. Zhan, Adv. Mater. **27**, 1170–1174 (2015)
5. J. Yuan, Y. Zhang, L. Zhou, G. Zhang, H.L. Yip, T.K. Lau, X. Lu, C. Zhu, H. Peng, P. Johnson, M. Leclerc, Y. Cao, J. Ulanski, Y. Li, Y. Zou, Joule **3**, 1140–1151 (2019)
6. Z. Zheng, J.Q. Wang, P.Q. Bi, J.Z. Ren, Y.F. Wang, Y. Yang, X.Y. Liu, S.Q. Zhang, J.H. Hou, Joule **6**, 171–184 (2021)
7. Y.F. Zhong, M. Causa, G.J. Moore, P. Krauspe, B. Xiao, F. Günther, J. Kublitski, R. Shivhare, J. Benduhn, E. BarOr, S. Mukherjee, K.M. Yallum, J. Réhault, S.C.B. Mannsfeld, D. Neher, L.J. Richter, D.M. DeLongchamp, F. Ortmann, K. Vandewal, E. Zhou, N. Banerji, Nat. Commun. **11**, 833 (2020)
8. C.L. He, Z. Chen, T.H. Wang, Z.Q. Shen, Y.K. Li, J.D. Zhou, J.W. Yu, H.Y. Fang, Y.H. Li, S.X. Li, X.H. Lu, W. Ma, F. Gao, Z.Q. Xie, V. Coropceanu, H.M. Zhu, J.-L. Bredas, L.J. Zuo, H.Z. Chen, Nat. Commun. **13**, 2598 (2022)
9. L. Zhu, M. Zhang, J.Q. Xu, C. Li, J. Yan, G.Q. Zhou, W.K. Zhong, T.Y. Hao, J.L. Song, X.N. Xue, Z.C. Zhou, R. Zeng, H.M. Zhu, C.-C. Chen, R.C.I. MacKenzie, Y.C. Zou, J. Nelson, Y.M. Zhang, Y.M. Sun, F. Liu, Nat. Mater. **21**, 656–663 (2022)
10. X. Guan, Y.F. Wang, S. Feng, J.D. Zhang, Q.Q. Yang, B.Y. Liu, D.S. Qin, Eur. Phys. J. Appl. Phys. **95**, 30201 (2021)
11. Y.H. Liu, B.W. Liu, C.-Q. Ma, F. Huang, G.T. Feng, H.Z. Chen, J.H. Hou, L.P. Yan, Q.Y. Wei, Q. Luo, Q.Y. Bao, W. Ma, W. Liu, W.W. Li, X.J. Wan, X.T. Hu, Y.C. Han, Y.W. Li, Y.H. Zhou, Y.P. Zou, Y.W. Chen, Y.F. Li, Y.S. Chen, Z. Tang, Z.C. Hu, Z.-G. Zhang, Z.S. Bo, Sci. China Chem. **65**, 224–268 (2022)
12. Y.H. Liu, B.W. Liu, C.-Q. Ma, F. Huang, G.T. Feng, H.Z. Chen, J.H. Hou, L.P. Yan, Q.Y. Wei, Q. Luo, Q.Y. Bao, W. Ma, W. Liu, W.W. Li, X.J. Wan, X.T. Hu, Y.C. Han, Y.W. Li, Y.H. Zhou, Y.P. Zou, Y.W. Chen, Y.F. Li, Y.S. Chen, Z. Tang, Z.C. Hu, Z.-G. Zhang, Z.S. Bo, Sci. China Chem. **65**, 1 (2022)
13. S. Gunes, H. Neugebauer, N.S. Sariciftci, Chem. Rev. **107**, 1324–1338 (2007)
14. G. Li, R. Zhu, Y. Yang, Nat. Photon. **6**, 153–161 (2012)
15. Y. Han, H. Dong, W. Pan, B. Liu, X. Chen, R. Huang, Z. Li, F. Li, Q. Luo, J. Zhang, Z. Wei, C.Q. Ma, A.C.S. Appl, Mater. Interfaces **13**, 17869–17881 (2021)
16. X. Xu, J. Xiao, G. Zhang, L. Wei, X. Jiao, H.L. Yip, Y. Cao, Sci. Bull. **65**, 208–216 (2020)
17. Y.Y. Jiang, X.Y. Dong, L.L. Sun, T.F. Liu, F. Qin, C. Xie, P. Jiang, L. Hu, X. Lu, X.M. Zhou, W. Meng, N. Li, C.J. Brabec, Y.H. Zhou, Nat. Energy **7**, 352–359 (2022)
18. Q. Kang, Q. Liao, C.Y. Yang, Y. Yang, B.W. Xu, J.H. Hou, Adv. Energy Mater. **12**, 2103892 (2022)
19. D.J.D. Moet, P. de Bruyn, J.D. Kotlarski, P.W.M. Blom, Appl. Phys. Lett. **96**, 153504 (2010)
20. C.X. Chen, P.Y. Xue, H. Lu, J.Y. Wang, B.Y. Jia, Y.W. Li, D.S. Qin, Y.Z. Lin, X.W. Zhan, Energy Technol. **9**, 2100281 (2021)
21. M. Kröger, S. Hamwi, J. Meyer, T. Riedl, W. Kowalsky, A. Kahn, Appl. Phys. Lett. **95**, 251 (2009)
22. D. Cheyns, B. Kam, K. Vasseur, P. Heremans, B.P. Rand, J. Appl. Phys. **113**, 043109 (2013)
23. D. Qin, H. Cao, C. Yan, S.S. Meng, J.X. Tang, X. Zhan, J. Mater. Chem. A **5**, 25385 (2017)
24. L. Hu, Y. Liu, L. Mao, S. Xiong, L. Sun, N. Zhao, Y. Zhou, J. Mater. Chem. A **6**, 2273–2278 (2018)
25. M.Y. Chan, S.L. Lai, K.M. Lau, C.S. Lee, S.T. Lee, Appl. Phys. Lett. **89**, 163515 (2006)
26. S. Feng, Z. Liu, H. Zhao, Q. Yang, J. Zhang, D. Qin, Eur. Phys. J. Appl. Phys. **97**, 55 (2022)
27. G.G. Malliaras, J.R. Salem, P.J. Brock, C. Scott, Phys. Rev. B **58**, R13411 (1998)
28. S.M.B. Ghorashi, A. Behjat, R. Ajeian, Sol. Energy Mater. Sol. Cells **96**, 50–57 (2012)
29. T. Kobori, T. Fukuda, Org. Electron. **51**, 76–85 (2017)
30. C. Stelling, C.R. Singh, M. Karg, T.A. König, M. Thelakkat, M. Retsch, Sci. Rep. **7**, 1–13 (2017)
31. Y. Yuan, D. Grozea, S. Han, Z. Lu, Appl. Phys. Lett. **85**, 4959–4961 (2004)
32. C. Cheng, Y. Chen, D. Qin, W. Quan, J. Liu, Chin. Phys. Lett. **11**, 117801 (2010)
33. I.S. Oh, C.H. Ji, S.Y. Oh, Electron. Mater. Lett. **1**, 156–162 (2016)
34. X. Guan, S. Feng, W. Liu, Y. Wang, D. Qin, Appl. Phys. A **127**, 1–6 (2021)
35. H. Wei, Q. Ou, Z. Zhang, J. Li, Y. Li, S. Lee, J. Tang, Org. Electron. **14**, 839–844 (2013)
36. Y.Q. Li, M.K. Fung, Z. Xie, S.T. Lee, L.S. Hung, J. Shi, Adv. Mater. **14**, 1317–1321 (2002)
37. K. Walzer, B. Maennig, M. Pfeiffer, K. Leo, Chem. Rev. **107**, 1233–1271 (2007)
38. S. Braun, W.R. Salaneck, M. Fahlman, Adv. Mater. **21**, 1450–1472 (2009)
39. P. Peumans, S.R. Forrest, Appl. Phys. Lett. **79**, 126–128 (2001)